Chemical Science

ROYAL SOCIETY OF CHEMISTRY

EDGE ARTICLE

View Article Online
View Journal | View Issue

Cite this: *Chem. Sci.*, 2025, **16**, 19956

Enhancing the reverse intersystem crossing (RISC) rates and efficiencies of MR-TADF emitters with a U-shaped molecular structure for solution-processed OLEDs

Shipan Xu,[a] Wenping Liu,[a] An Yan,[a] Xuyang Du,[a] Yuanhui Sun, *[a] Junfei Tao,[a] Guijiang Zhou,*[a] Zhao Chen *[b] and Xiaolong Yang *[a]

Received 19th June 2025
Accepted 19th September 2025

DOI: 10.1039/d5sc04507j

rsc.li/chemical-science

Multi-resonance thermally activated delayed fluorescence (MR-TADF) emitters hold great potential for applications in organic light-emitting diodes (OLEDs). However, owing to their inherently rigid and planar molecular structures and the localized charge transfer (LCT) characteristics, these emitters typically exhibit poor solubility and low reverse intersystem crossing (RISC) rates, which are unfavorable for high-performance solution-processed OLEDs. Herein, we constructed three U-shaped MR-TADF emitters (BN-N-TTz, BN-N-PCz and BN-N-BN) by introducing triazine, phenylcarbazole and MR-TADF units at the 1- and 8-positions of a naphthalene ring. This U-shaped molecular architecture endows the emitters with excellent solubility. Moreover, this structure not only enhances spin–orbit coupling between the S_1 and T_1 states but also reduces the energy difference between the two states (ΔE_{ST}), thereby increasing RISC rates to as high as 3.17×10^5 s^{-1}. Notably, the solution-processed OLED based on BN-N-BN achieved the highest EQE of 27.6% without sensitizers. This represents one of the best performances among solution-processed OLEDs based on MR-TADF emitters to date. This simple approach reveals the great potential for developing solution-processable emitters suitable for high-performance rigid and planar molecular structures.

Introduction

Organic light-emitting diode (OLED) display technology, characterized by its ultra-lightweight, flexibility, thinness, low power consumption, wide viewing angle, self-luminosity, and vibrant colors, holds great application potential in the fields of full-color displays and solid-state lighting.[1–5] Solution-processed OLEDs offer several advantages over vacuum-deposited OLEDs, such as low-cost manufacturing, simplified preparation procedures and suitability for large-area production and flexible substrates.[6,7] One of the keys to achieving high performance in solution-processed OLEDs is to develop emitters with both good solubility and excellent luminescent properties. Multi-resonance thermally activated delayed fluorescence (MR-TADF) emitters containing boron and nitrogen atoms have garnered extensive attention from both academic and commercial circles in the OLED display field due to their superior luminescent properties, such as high color purity, narrowband emission, and high efficiency.[8–12] These emitters feature electron-deficient centers (boron atoms) and electron-rich centers (nitrogen atoms) with opposite resonance effects. This design enables the highest occupied molecular orbital (HOMO) and the lowest unoccupied molecular orbital (LUMO) to localize on different atoms within the molecular framework, thereby achieving a small singlet-triplet energy gap (ΔE_{ST}) and exhibiting TADF characteristics.[13] Compared with traditional donor–acceptor type TADF materials, MR-TADF materials possess rigid structures and LCT characteristics, which are conducive to achieving high color purity with narrow-band emission and high photoluminescence quantum yields (PLQYs).[14] Recently, a plethora of top-tier MR-TADF emitters have been constructed through various ingenious molecular design methodologies.[15–21] For example, Adachi *et al.* developed a pure blue MR-TADF emitter which showed a fast RISC rate without the use of heavy atoms.[22] Wang *et al.* reported two narrowband deep-blue MR-TADF emitters by using the nitrogen atom embedding strategy.[23] Duan *et al.* demonstrated the first implementation of easy-to-access MR-TADF emitters with B–N covalent bonds.[24] However, most MR-TADF emitters often suffer from poor solubility due to their inherent rigid planar

---

[a] *School of Chemistry, Xi'an Key Laboratory of Sustainable Energy Material Chemistry, Engineering Research Center of Energy Storage Materials and Devices, Ministry of Education, Xi'an Jiaotong University, Xi'an 710049, China. E-mail: sunyuanhui@xjtu.edu.cn; zhougj@xjtu.edu.cn; xiaolongyang@xjtu.edu.cn*

[b] *Key Laboratory of Basic Pharmacology of Ministry of Education and Joint International Research Laboratory of Ethnomedicine of Ministry of Education, School of Pharmacy, Zunyi Medical University, Zunyi, 563000, China. E-mail: chenzhao2006@163.com*

structures, leading to more applications in vacuum thermal evaporation for device fabrication. In addition, during the vacuum thermal evaporation process, these emitters are predominantly doped into the host matrix at low concentrations, typically ranging from 0.5 wt% to 1 wt%. Achieving precise control over such low doping levels is highly difficult and thus significantly increases the difficulty of device fabrication. Therefore, research on fabricating high-performance solution-processed OLEDs based on MR-TADF is full of challenges. Encouragingly, a number of studies have already reported external quantum efficiencies (EQEs) exceeding 20% using solution-processible MR-TADF emitters. For example, based on MR-TADF emitters, Hatakeyama *et al.* developed a solution-processed pure green OLED with a high EQE of 21.8% (λ_{EL} = 506 nm),[25] Wang *et al.* demonstrated a high-performance solution-processable pure-red OLED with an EQE of 20.1%,[26] and Yang *et al.* increased the EQE of a solution-processed bluish-green OLED up to 27.1% (λ_{EL} = 495 nm).[27] Nonetheless, due to the poor solubility and film-forming properties of most MR-TADF materials, the MR-TADF emitters prepared by solution processes still lag behind those fabricated *via* vacuum deposition. The efficiency of solution-processed OLEDs based on MR-TADF emitters is generally low. Furthermore, the majority of MR-TADF emitters have long been troubled by low RISC rates, limiting their further application.[28–30] Although the use of sensitizers can indirectly circumvent this issue, it inevitably increases costs. Therefore, developing solution-processible MR-TADF emitters with high efficiency and high RISC rates remains a challenge.

Herein, we designed and synthesized three solution-processible MR-TADF emitters with a U-shaped molecular structure, namely BN-N-TTz, BN-N-PCz and BN-N-BN, by introducing triazine, phenylcarbazole and MR-TADF units at the 1- and 8-positions of the naphthalene ring (Scheme 1). We selected the bluish-green emitter of BNCz as the core for multiple resonance (MR) emission, given its straightforward synthesis and superior electroluminescence (EL) performance. The U-shaped molecular structure enhances the solubility of the three emitters. In addition, the enhanced spin–orbit coupling between the S_1 and T_1 states of these three emitters results in a higher rate of RISC compared to BNCz, especially for BN-N-BN, where the RISC rate reaches 3.17×10^5 s^{-1}. As we anticipated, the solution-processed OLED achieved good performances with an EQE_{max} of 25.2% and a FWHM of 28 nm (0.14 eV) for BN-N-TTz, and an EQE_{max} of 19.5% and a FWHM of 28 nm (0.14 eV) for BN-N-PCz. For BN-N-BN, the solution-processed green OLED achieved excellent performance with an EQE_{max} of 27.6%.

Results and discussion

The molecular design strategy of these BN-based emitters, BN-N-TTz, BN-N-PCz and BN-N-BN, is illustrated in Scheme 2 and S1. The details of the synthetic methods for these BN-based emitters are provided in the SI. We primarily synthesized these three target compounds *via* a straightforward Suzuki-coupling reaction. The chemical structures of BN-N-TTz, BN-N-PCz and BN-N-BN were evaluated by nuclear magnetic resonance (NMR) and high-resolution mass spectrometry (HRMS) spectra (Fig. S1 and S2). Notably, these emitters exhibit good solubility in common solvents such as dichloromethane, tetrahydrofuran, and chlorobenzene, which is a significant improvement over BNCz. This suggests their potential as emitters for solution-processed OLEDs. Their thermal stabilities were estimated by thermogravimetric analysis (TGA). The TGA curves suggested that decomposition temperatures (T_d) of these emitters were in the range of 446–503 °C (Fig. S3 and Table 1), demonstrating sufficient thermal stability for the device fabrication processes and practical usages. Based on the cyclic voltammetry tests (Fig. S4), the HOMO energy levels of

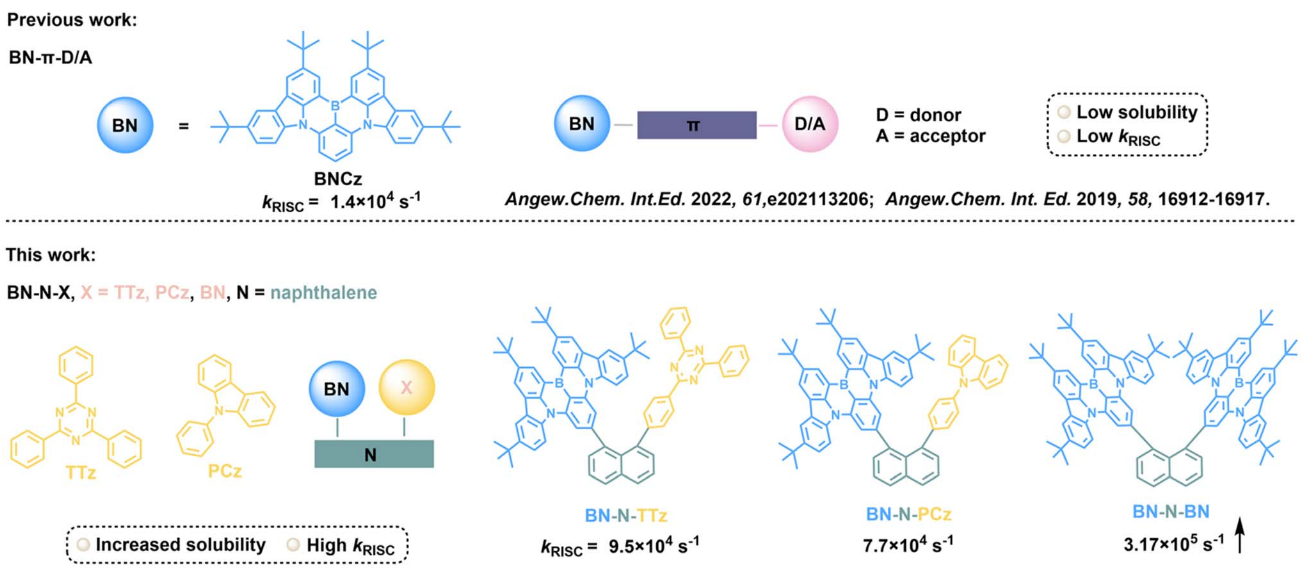

Scheme 1 Molecular design concept and chemical structures of these U-shaped emitters.

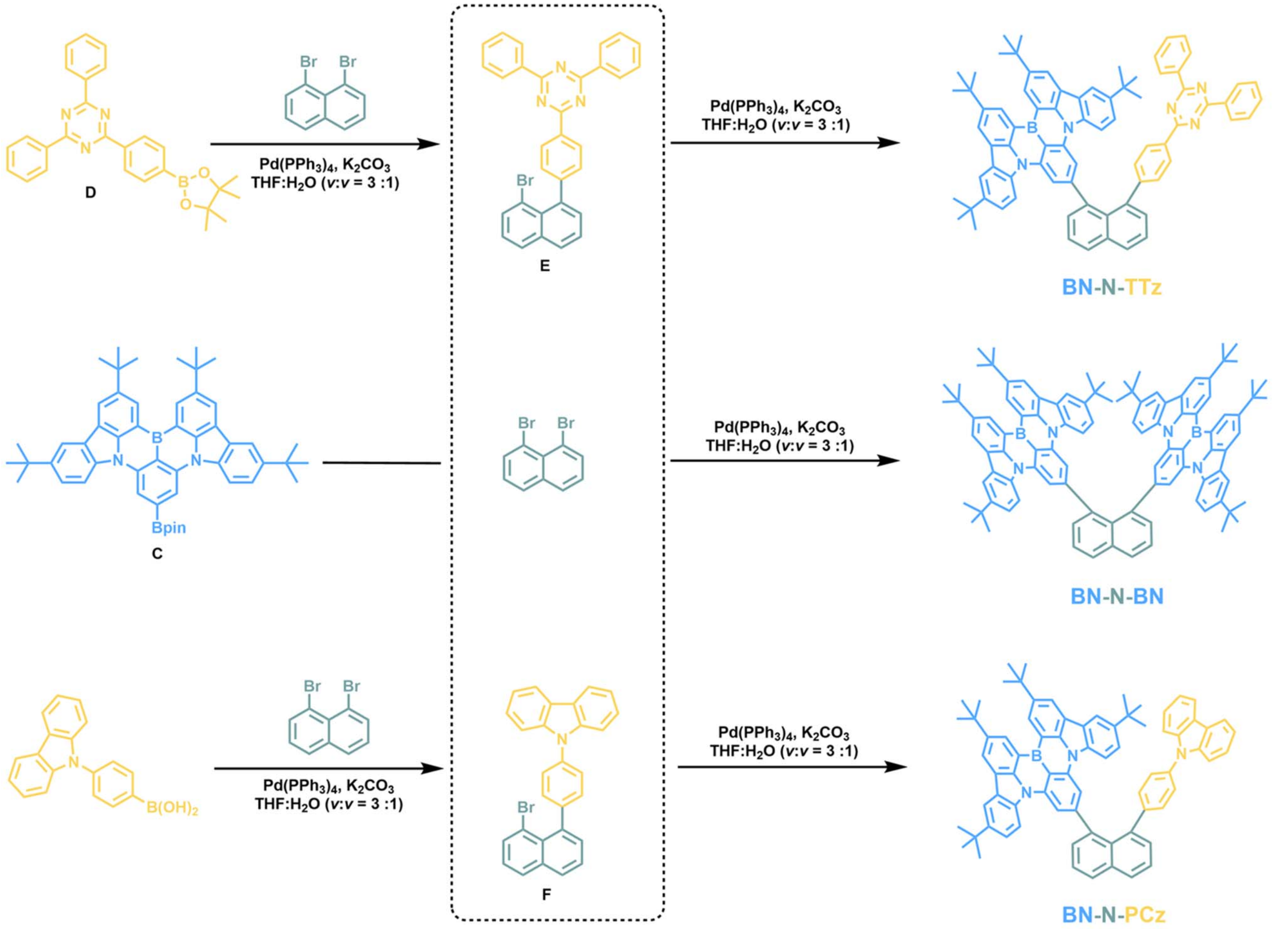

Scheme 2 Synthetic routes of BN-N-TTz, BN-N-PCz and BN-N-BN.

BN-N-TTz, BN-N-PCz and BN-N-BN were deduced to be −5.49, −5.53 and −5.31 eV, respectively. Meanwhile, their energy band gaps (E_g) estimated from the onset of absorption spectra in solutions are 2.57, 2.58, and 2.41 eV. Thereby, the LUMO levels of these three emitters were determined to be −2.92, −2.95, and −2.90 eV, respectively.

The molecular structures of BN-N-TTz and BN-N-PCz optimized through DFT simulation exhibit highly twisted, folded, and bulky geometric structures, which are almost identical to their geometric structures in the single-crystal state (Fig. 1). For BN-N-TTz and BN-N-PCz, the torsion angles between the bridge naphthalene and acceptor triazine/donor phenylcarbazole/fluorophore BNCz (α_1/α_2) are 53.2°/61.3° and 54.4°/61.4°, respectively. The entire π-framework is no longer a single continuous plane but is instead bent into three segments with mutual dihedral angles of approximately 60°. Each molecule can present less than 40% of its π-surface for ideal face-to-face stacking, which markedly weakens the driving force for π–π aggregation. The distorted torsion angles arising from different intramolecular moieties lead to highly twisted geometrical structures and significant steric hindrance effects. These findings collectively favor a pronounced enhancement in the

Table 1 Photophysical, thermal, and electrochemical data for BN-N-TTz, BN-N-PCz and BN-N-BN

Emitter	$\lambda_{abs}{}^a$ [nm]	$\lambda_{em}{}^a$ [nm]	FWHM^b [nm eV^{-1}]	$E_{HOMO}{}^c/E_{LUMO}{}^d$ [eV]	$E_{S1}/E_{T1}{}^e$ [eV]	$\Delta E_{ST}{}^f$ [eV]	T_d (°C)
BN-N-TTz	476	495	25/0.11	−5.49/−2.92	2.61/2.46	0.15	457
BN-N-PCz	476	493	25/0.11	−5.53/−2.95	2.64/2.47	0.17	446
BN-N-BN	462	537	59/0.25	−5.31/−2.90	2.48^g, 2.37^h/2.34	0.14^g/0.03^h	503

[a] Measured at a concentration of *ca.* 10^{-5} M in toluene at room temperature. [b] Full-width at half-maximum. [c] Determined by cyclic voltammetry in CH_2Cl_2 solution. [d] Deduced from the E_{HOMO} and the optical energy gap (E_g) values. [e] Singlet (E_{S_1}) and triplet (E_{T_1}) excited energies estimated from the PL spectra at 77 K and phosphorescence spectra at 77 K in solution, respectively. [f] $\Delta E_{ST} = E_{S_1} - E_{T_1}$. [g] S_1 state, *i.e.*, BNCz monomers in BN-N-BN. [h] S_{exc} state.

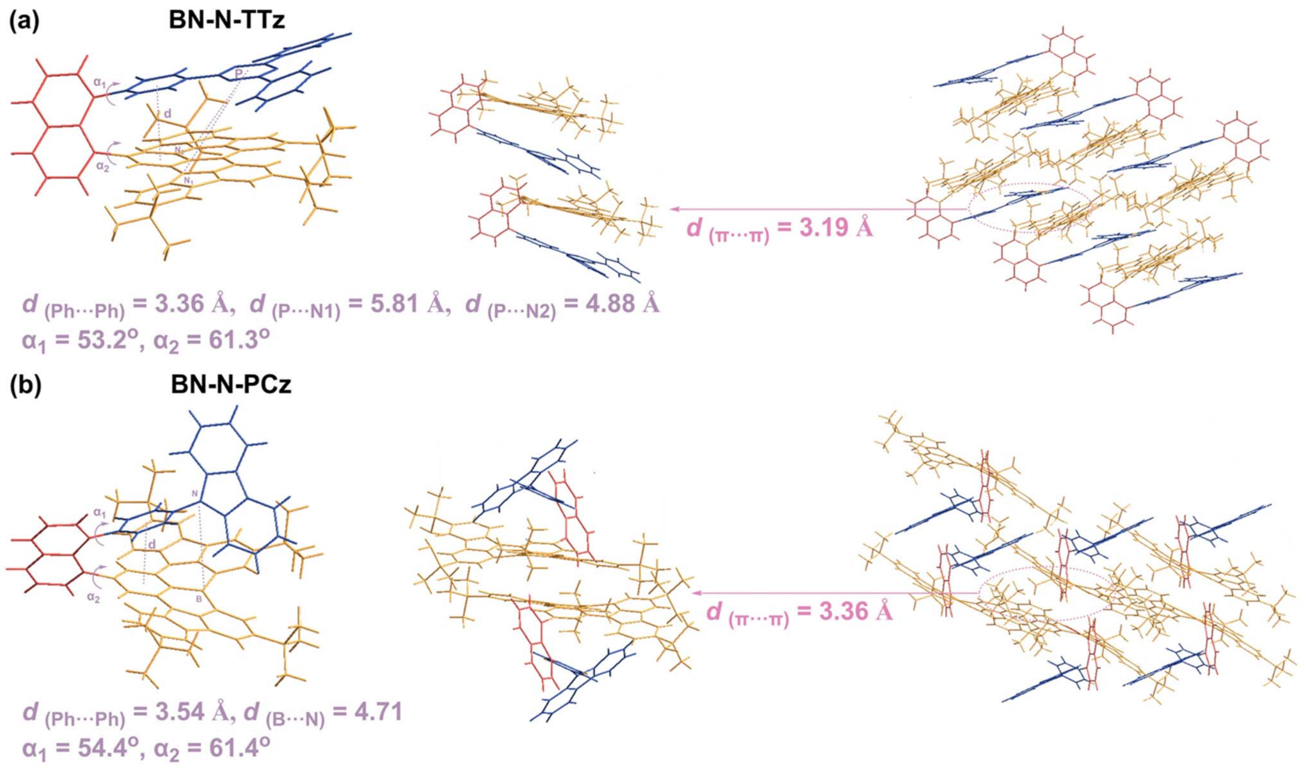

Fig. 1 Crystal structures and packing modes of (a) BN-N-TTz and (b) BN-N-PCz.

solubility of compounds BN-N-TTz and BN-N-PCz. Notably, the distances between the centroids of the two phenyl rings directly connected to the bridge naphthalene ($d_{(\text{Ph}\cdots\text{Ph})}$s) in these two molecules are within 3.6 Å. The distances between the nitrogen atom on the fluorophore BNCz and the triazine receptor center of BN-N-TTz are 5.81 ($d_{(\text{P}\cdots\text{N1})}$s) and 4.88 Å ($d_{(\text{P}\cdots\text{N2})}$s), respectively. For BN-N-PCz, the distance between the boron atom on the fluorophore BNCz and the nitrogen atom on the donor phenylcarbazole is 4.71 Å ($d_{(\text{B}\cdots\text{N})}$). These results indicate that the donor phenylcarbazole or the acceptor triazine and the fluorophore BNCz are spatially distant from each other, almost in an isolated state, making it difficult for direct electron exchange and transition to occur when subjected to external light/electric field excitation. Therefore, under this premise, the introduction of the donor phenylcarbazole or the acceptor triazine hardly affects the emission color of the original fluorescent chromophore BNCz. In addition, the crystal structure of BN-N-TTz exhibits an intermolecular layer-by-layer staggered arrangement between the fluorophore BNCz. While in the crystal packing of BN-N-PCz, although π–π overlaps are discernible, the overlapping area is sterically "elevated" by the flanking phenyl/carbazole substituents, thereby diminishing the effective contact. The loose packing modes observed in the crystals of both molecules effectively suppress π–π aggregation between the BNCz cores, thereby facilitating enhanced solubility of these compounds. Unfortunately, despite numerous attempts at growing single crystals of compound BN-N-BN, we have been unable to obtain high-quality single crystals for testing and analysis.

In order to investigate the frontier molecular orbital (FMO) distributions and ground state geometry configurations, density functional theory (DFT) calculations were carried out on the model compounds BN-N-TTz, BN-N-PCz and BN-N-BN (Fig. 2). For BN-N-TTz, the HOMO is primarily distributed on the nitrogen atoms in the carbazole and its *ortho*/*para* carbon atoms, while the LUMO is mainly distributed on the triazine moiety and the boron atom, along with its *ortho*/*para* carbon atoms, with a small portion distributed on the naphthalene ring. Such a spatial separation implies a charge-transfer (CT) character for the S_1–S_0 transition. The HOMO of BN-N-PCz is primarily distributed on the nitrogen atoms of the carbazole in the BN core and their *ortho*/*para* carbon atoms, with a portion distributed on the nitrogen atoms of the carbazole opposite the BN core, while the LUMO is predominately distributed on the boron atoms and carbon atoms at their *ortho*/*para* positions, with a small portion distributed on the naphthalene ring. However, the FMOs of BN-N-BN are primarily dominated by resonance, with a small portion of the LUMO still distributed on the naphthalene ring.

To investigate whether the BNCz core in these three emitters undergoes through-space CT with the triazine acceptor, the phenylcarbazole donor, or other BNCz units, the intramolecular non-covalent interactions (NCIs) were investigated by utilizing the independent gradient model based on Hirshfeld partition of molecular density (IGMH) based on their optimized structures (Fig. 3). The results indicate that the NCIs are predominantly present between the two phenyl rings that are directly linked to the bridging naphthalene. These interactions represent

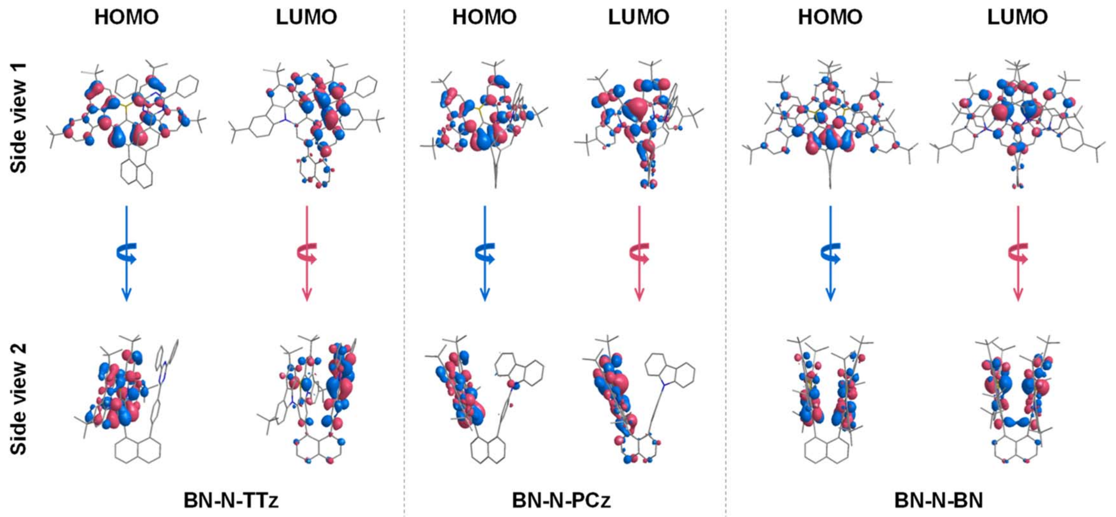

Fig. 2 HOMO and LUMO distributions calculated based on the optimized structures.

significant intramolecular van der Waals forces and exert a strong steric hindrance effect, thereby making it difficult for effective space charge transfer behavior to occur.

To elucidate the electronic characteristics of molecules BN-N-TTz, BN-N-PCz and BN-N-BN, density functional theory (DFT) and time-dependent DFT (TD-DFT) calculations were used to calculate hole and electron distributions, and spin–orbit coupling matrix elements ($<\mathrm{S}|\hat{H}_{\mathrm{SOC}}|\mathrm{T}>\mathrm{s}$) (Fig. 4). In the natural transition orbital (NTO) distributions of S_1, the hole distributions for BN-N-TTz are mainly located on the BNCz skeleton. However, the electron distribution differs markedly from that of the LUMO, being concentrated mainly on the BNCz core with only a minor extension onto the naphthalene ring. The LUMO corresponds to an eigenfunction of the ground-state

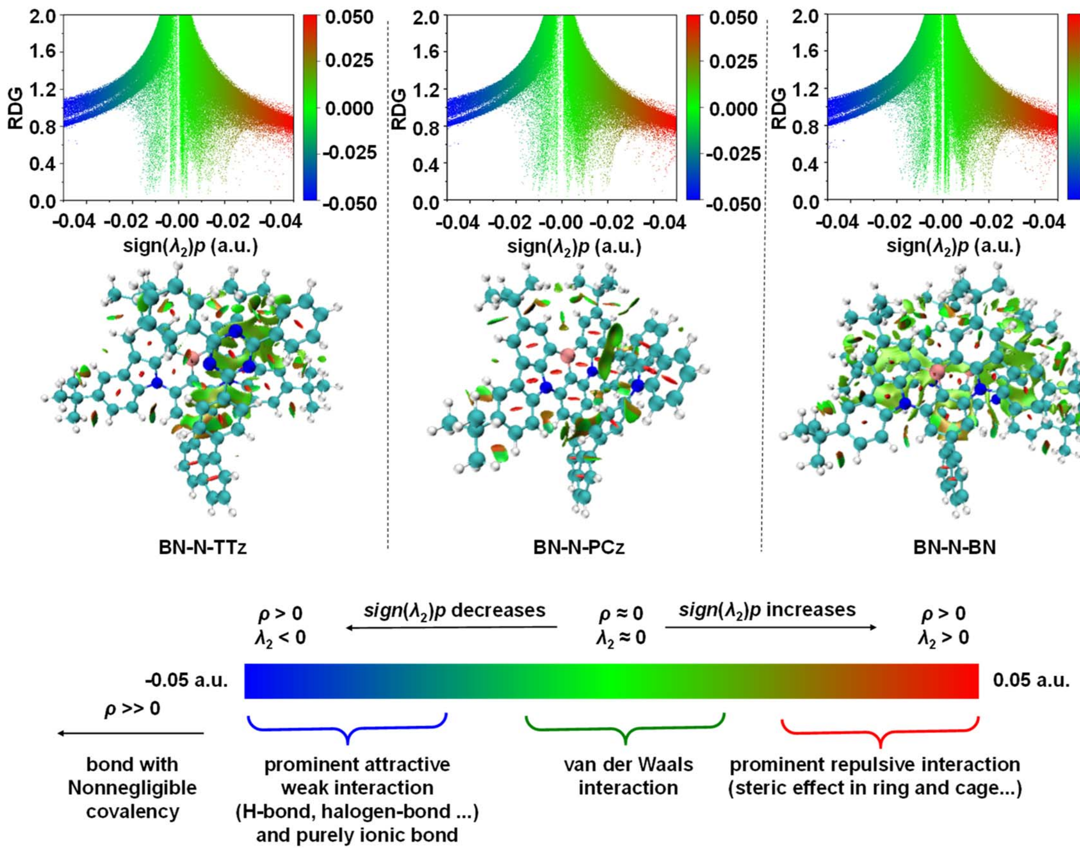

Fig. 3 Calculated reduced density gradient (RDG) isosurfaces and scattering diagrams.

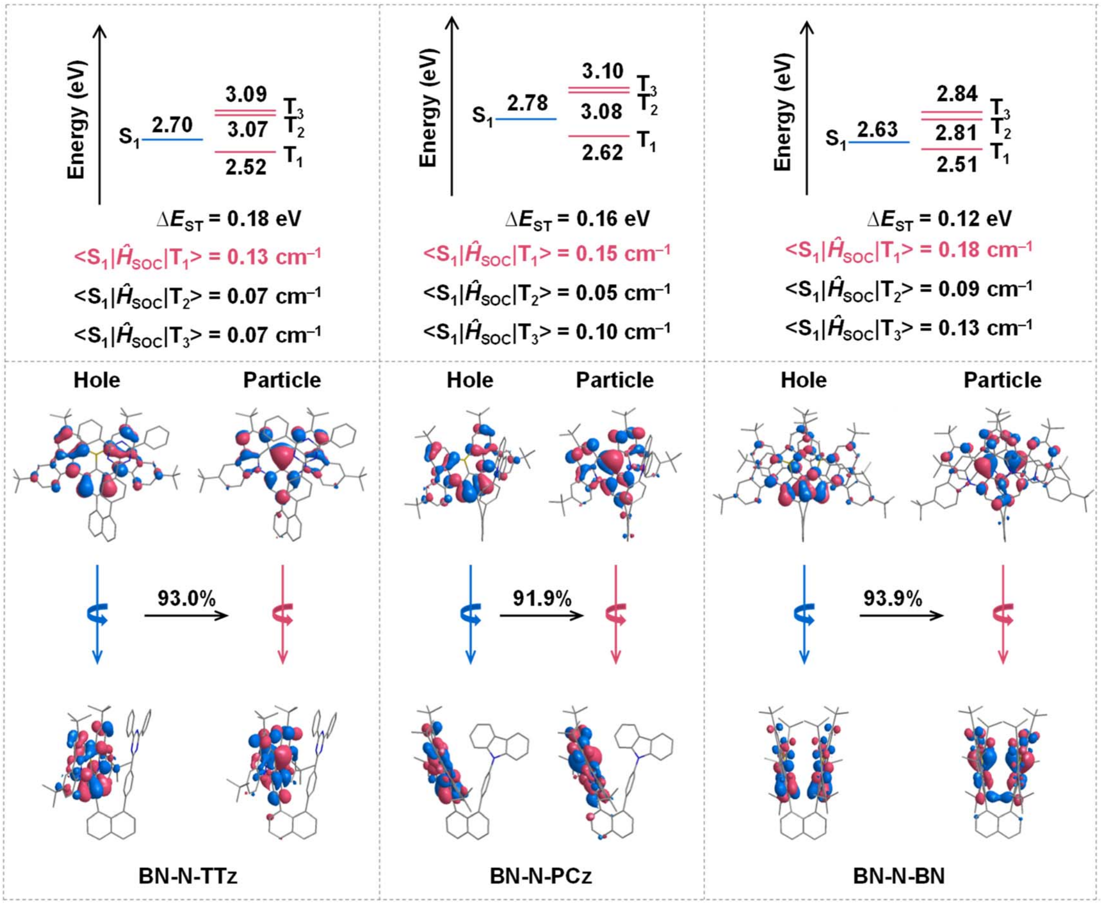

Fig. 4 Energy levels of excited states and hole/particle orbital distributions of S_0 to S_1.

Fock/Kohn–Sham operator, whereas the NTO particle constitutes an eigenfunction of the transition-density matrix and is consequently excitation-specific. Owing to the delocalized character of the ground-state virtual manifold and its admixture *via* configuration interaction, the NTO particle is generally expressed as a linear combination of multiple canonical virtual orbitals. In this instance, the contribution coefficient of the canonical LUMO is small, thereby attenuating its spatial signature. Accordingly, the electron NTO may exhibit a distribution distinct from that of the LUMO. Actually, the hole distributions for these emitters are mainly located on the BNCz skeleton. For the electron distributions of the three molecules, apart from the fluorophore BNCz, a portion of the electron distribution extends to the naphthalene ring directly connected to the BNCz fluorophore. This further indicates that there is no through-space charge transfer (CT) between the BN units and the carbazole donor or triazine acceptor. Such results also explain why BN-N-TTz and BN-N-PCz exhibit similar emission wavelengths. In addition, we examined the natural transition orbitals of the T_1–T_3 states for these emitters (Fig. S5–S7). The results reveal that T_1 and S_1 share similar excited-state characteristics, whereas T_2 and T_3 exhibit markedly different excitation features. Notably, due to the strong π-conjugation extension between the bridging naphthalene and the BNCz fluorophore in BN-N-X, there is a charge transfer between the carbazole donor unit in the BNCz core and the bridging naphthalene acceptor, which is likely responsible for the enhanced SOC between the S_1 and T_1 states.[16]

To investigate the photophysical properties of the three emitters, the UV-vis absorption and photoluminescence (PL) spectra were measured, as shown in Fig. 5, and the detailed photophysical data are summarized in Table 1. The absorption bands of compounds BN-N-TTz, BN-N-PCz and BN-N-BN below 400 nm are assigned to *n*–π* and π–π* transitions, while the intense absorption peaks at 476, 476, and 462 nm, respectively, are ascribed to the LCT transition absorption of the BN unit. For emitters BN-N-TTz and BN-N-PCz, exhibited emission peaks at 495 and 493 nm, respectively, with narrow full widths at half maximum (FWHMs) of 25 nm (0.11 eV) and tiny Stokes shifts of 19 and 17 nm (0.10 and 0.09 eV), reflecting the minimal structure relaxations during the emission process after light excitation. However, the emission peak of BN-N-BN has redshifted to 537 nm, featuring a relatively large FWHM of 59 nm (0.25 eV) and a significant Stokes shift of 75 nm (0.11 eV). This is primarily due to the characteristics of the co-facial dimer structure resembling an excimer-like state (S_{exc}).[31] By varying the solutions from *n*-hexane to DMF, for BN-N-TTz and BN-N-PCz, the FWHMs remained largely unchanged, and a weak positive solvatochromic effect was observed, indicating the insensitivity of environment polarity due to the relatively weak

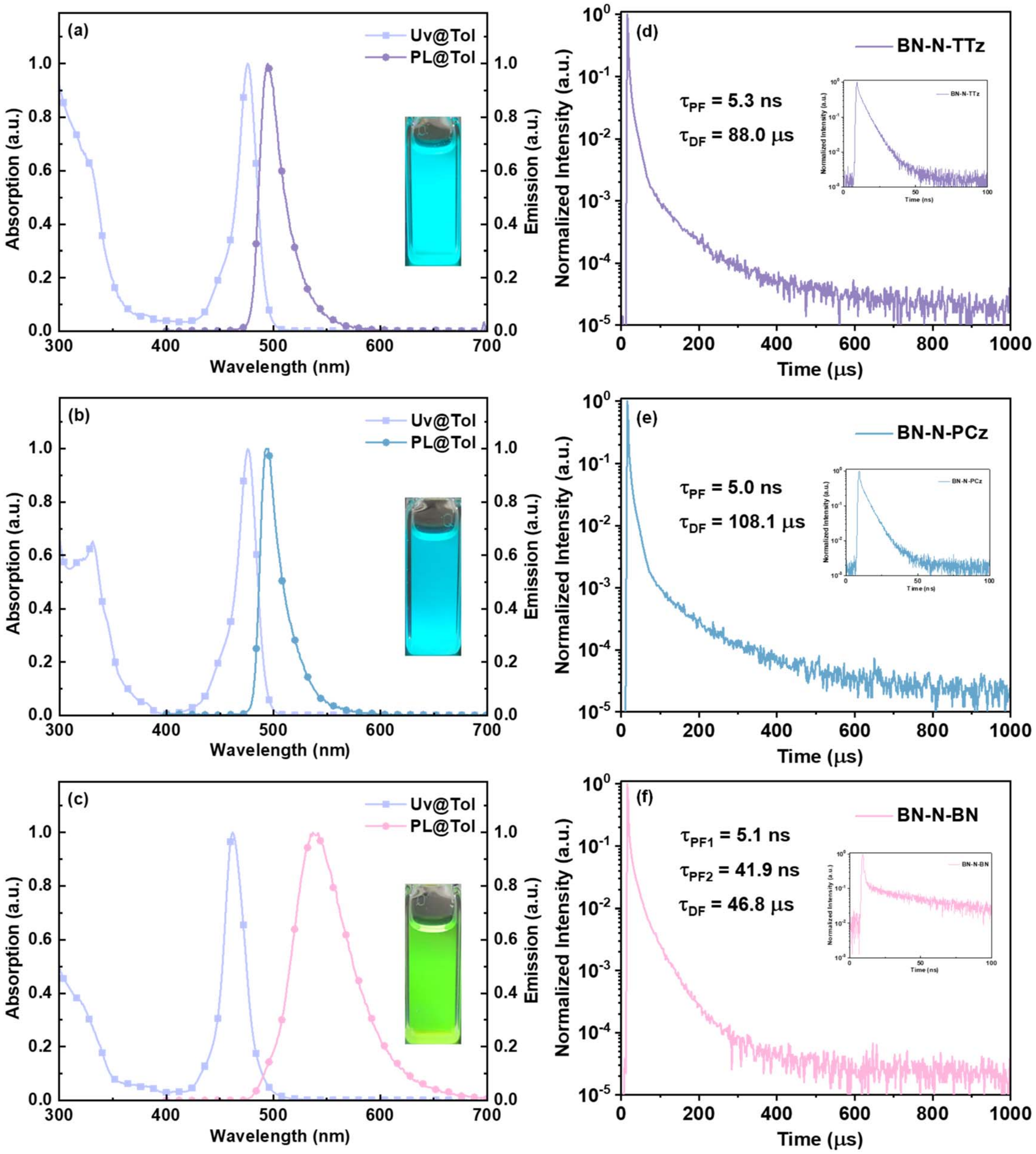

Fig. 5 Normalized UV-vis absorption and fluorescence spectra of (a) BN-N-TTz, (b) BN-N-PCz, and (c) BN-N-BN, measured in toluene solution (1×10^{-5} M). (Inset in (a–c): photograph taken under 365 nm UV light). Transient PL decay spectra measured in a film doped with 1 wt% emitters in CBP (d–f).

intramolecular CT interaction (Fig. S8). In contrast, for the emitter BN-N-BN, no discernible positive solvatochromic effect was detected, further demonstrating its even weaker intramolecular charge-transfer character. This difference is likely attributable to the formation of an excimer-like state. In addition, k_{RISC} is highly dependent on ΔE_{ST} and the corresponding spin–orbit coupling effect. To estimate ΔE_{ST}, determined from the onset wavelengths of fluorescence and phosphorescence spectra in dilute toluene solution at 77 K, BN-N-TTz and BN-N-PCz possessed S_1/T_1 energy levels of 2.61/2.46 and 2.64/2.47 eV, respectively, giving the relatively small ΔE_{ST} values of 0.15/0.17 eV. For BN-N-BN, we calculated the fluorescence emission peak and phosphorescence emission peak at low temperatures, yielding ΔE_{ST} and $\Delta E_{\mathrm{S(exc)T}}$ values of 0.14 and 0.03 eV, respectively (Fig. S9 and Table 1). Such small ΔE_{ST} values promise an efficient RISC process with ambient thermal energy. In addition, the $<S_1|\hat{H}_{\mathrm{SOC}}|T_1>$ values between the S_1 state and T_1 states of BN-N-TTz ($<S_1|\hat{H}_{\mathrm{SOC}}|T_1> = 0.13\ \mathrm{cm}^{-1}$), BN-N-PCz ($<S_1|\hat{H}_{\mathrm{SOC}}|T_1> = 0.15\ \mathrm{cm}^{-1}$) and BN-N-BN ($<S_1|\hat{H}_{\mathrm{SOC}}|T_1> = 0.18\ \mathrm{cm}^{-1}$) are increased by 4 to 6 times compared with those reported for BNCz ($<S_1|\hat{H}_{\mathrm{SOC}}|T_1> = 0.03\ \mathrm{cm}^{-1}$),[32,33] indicating greatly enhanced spin–orbit coupling effect of BN-N-TTz, BN-N-PCz and BN-N-BN, which can facilitate the enhancement of k_{RISC} (Table S1). These results fully demonstrate that our strategy of

Table 2 Photophysical data of BN-N-TTz, BN-N-PCz and BN-N-BN in 1 wt% doped CBP

Emitter	λ_{em}[a] [nm]	FWHM[b] [nm eV^{-1}]	PLQY[c] [%]	τ_{PF}[d] [ns]	τ_{DF}[d] [μs]	k_{r}[e] [10^7 s^{-1}]	k_{nr}[e] [10^7 s^{-1}]	k_{RISC}[f] [10^4 s^{-1}]
BN-N-TTz	493	27/0.14	91	5.3	88.0	16.6	1.5	9.5
BN-N-PCz	492	28/0.14	87	5.0	108.1	16.4	2.1	7.7
BN-N-BN	500[g]/533[h]	66/0.29	93	5.1[g]/41.9[h]	46.8	1.5	0.1	31.7

[a] Measured in a doped film of 1 wt% emitters in CBP at room temperature. [b] Full-width at half-maximum. [c] Absolute PL quantum yields were evaluated in the doped film of 1 wt% emitters in CBP using an integrating sphere under a N_2 atmosphere. [d] The prompt fluorescence (τ_{PF}) and delayed fluorescence (τ_{DF}) lifetime. [e] The radiative rate constant (k_{r}) and non-radiative rate constant (k_{nr}) of S_1 to S_0 and the rate constant of reverse intersystem crossing (k_{RISC}). [f] Intersystem crossing (ISC) and reverse intersystem crossing (RISC) rates between S_1 and T_1 states. [g] τ_{PF} of the S_1 state, *i.e.*, BNCz monomers in BN-N-BN. [h] τ_{PF} of the S_{exc} state.

adopting a U-shaped molecular structure to promote the RISC process is successful.

In the doping films with 4,4′-Bis(*N*-carbazolyl)-1,1′-biphenyl (CBP) as the host material, BN-N-TTz and BN-N-PCz displayed narrowband emissions with emission peaks of 493 and 492 nm and FWHMs of 27 and 28 nm (0.14 eV), respectively. Additionally, BN-N-BN exhibited broader emission with a main emission peak at 533 nm and a shoulder peak at 500 nm, with an FWHM of 66 nm (0.29 eV) (Fig. S10 and Table 2). The transient PL decay spectra were measured to investigate the TADF characteristics of the three emitters. For BN-N-TTz and BN-N-PCz, the prompt fluorescence lifetimes (τ_{PF}) of below 6.0 ns and delayed fluorescence lifetimes (τ_{DF}) of 88.0 μs and 108.1 μs, respectively, were detected in their doping films. Meanwhile, BN-N-BN exhibited biexponential fluorescence decay in the CBP-doped film ($\tau_{\text{PF1}} = 5.1$ ns and $\tau_{\text{PF2}} = 41.9$ ns). More specifically, the emission at 500 nm is predominantly characterized by a fast decay ($\tau_{\text{PF1}} = 5.1$ ns), which is attributed to the lifetime of the S_1 state. Concurrently, a slower decay ($\tau_{\text{PF2}} = 49$ ns) is observed, corresponding to the S_{exc} at 533 nm (Fig. S10). This slow decay aligns with the extended lifetimes typically associated with excimer-like states as reported in previous studies.[34,35] In addition, BN-N-BN has a relatively short delayed fluorescence lifetime of 46.8 μs. In the doping films of 1 wt% emitters, the absolute PLQYs of BN-N-TTz, BN-N-PCz and BN-N-BN are as high as 91%, 87%, and 93%, respectively. Across the three emitters, the radiative rate constants k_{r} are 16.6×10^7 s^{-1} (BN-N-TTz), 16.4×10^7 s^{-1} (BN-N-PCz) and 1.5×10^7 s^{-1} (BN-N-BN). These values fall within the typical range reported for MR-TADF fluorophores (10^6–10^8 s^{-1}). Notably, BN-N-BN exhibits the lowest k_{r} of the series, which is attributed to the long fluorescence lifetime of the S_{exc}. They possess considerably high k_{r} values, which are much greater than the k_{nr} values. This indicates a rapid radiative transition rate, reflected in the high PLQYs of their corresponding doped films. Their k_{RISC} values are 9.5, 7.7 and 31.7 × 10^4 s^{-1}, respectively. According to Fermi's golden rule, the k_{RISC} is related to SOC matrix elements and the S_1–T_1 energy gap (ΔE_{ST}). It is evident that the k_{RISC} of BN-N-BN is significantly higher than that of BN-N-TTz and BN-N-PCz, attributed to its enhanced SOC and small ΔE_{ST}. The greatly enhanced SOC may be the main reason for the intrinsic TADF of BN-N-BN.[31] Meanwhile, as the S_{exc} state is energetically lower than the S_1 state of BN-N-BN, the resulting ΔE_{ST} (T_1–S_{exc}) = 0.03 eV may also contribute to the observed k_{RISC} of 31.7×10^4 s^{-1} in the CBP-doped film. It is worth noting that the k_{RISC} values of these three luminescent materials are much higher than those reported for BNCz in the previous literature.[33] In other words, the rate of triplet exciton upconversion is higher in BN-N-TTz, BN-N-PCz and BN-N-BN (Fig. 6).

Due to the good solubility of these emitters in common organic solvents, BN-N-TTz, BN-N-PCz and BN-N-BN were used to fabricate solution-processed OLEDs with the device structure of indium tin oxide (ITO)/poly(3,4-ethylenedioxythiophene):polystyrene sulfonate (PEDOT:PSS, 30 nm)/poly(9-vinylcarbazole) (PVK) (35 nm)/1.0 wt% emitters: 4,4′-Bis(*N*-carbazolyl)-1,1′-biphenyl (CBP) (30 nm)/1,3,5-tri(*m*-pyridin-3-ylphenyl)benzene (TmPyPB) (40 nm)/LiF (1 nm)/Al (100 nm) (Fig. 7). Here, compounds PEDOT:PSS, PVK, CBP, TmPyPB and LiF served as hole-injection, hole-transporting, host, electron-transporting and electron-injection materials,

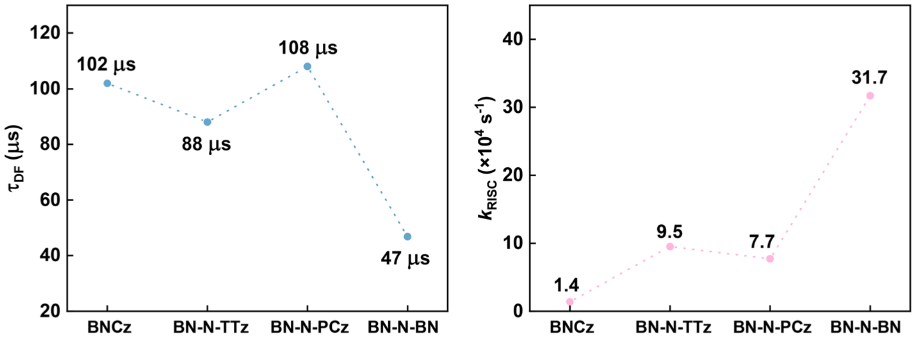

Fig. 6 Delayed fluorescence (τ_{DF}) lifetime and RISC rate constant (k_{RISC}). Collected from values reported in ref. 27 (BNCz).

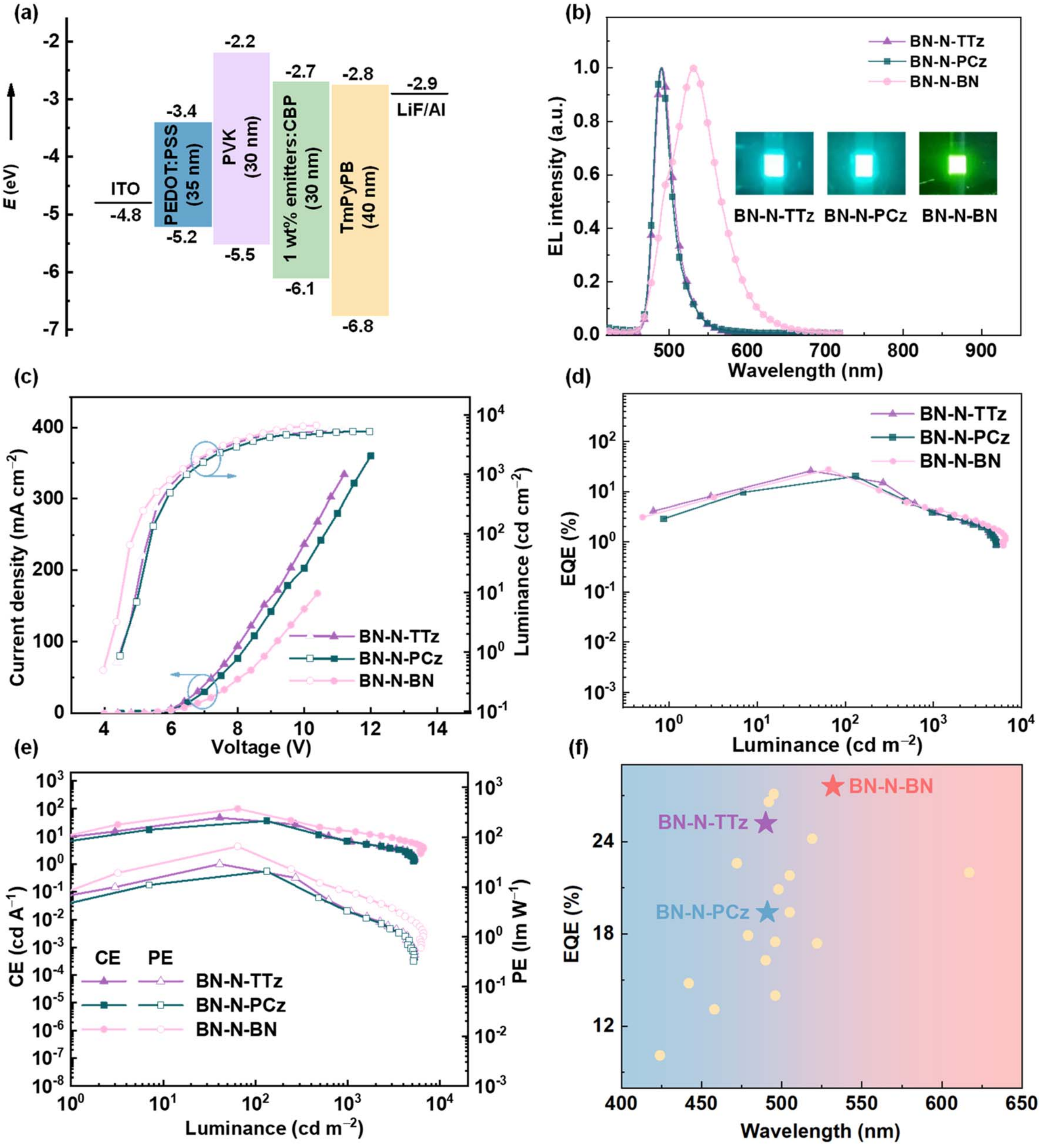

Fig. 7 (a) Device structure. (b) EL spectra of the device (inset: photograph of solution-processed OLEDs based on BN-N-TTz, BN-N-PCz and BN-N-BN). (c) Current density (*J*)–voltage (*V*)-luminance (*L*) curves. (d) EQE *versus* luminance characteristics. (e) CE or PE *versus* luminance characteristics. (f) Maximum EQE of solution-processed OLEDs based on MR-TADF emitters without sensitizers.

respectively. The molecular structures of these functional materials used in the fabricated OLEDs are shown in Fig. S11. The resultant device performances including EL spectra, the current density (*J*)–voltage (*V*)–luminance (*L*) curves, and the relationship between EQEs or current efficiency (CE) or power efficiency (PE) and luminance are depicted in Fig. 7. The related key EL data are summarized in Table 3.

The devices based on BN-N-TTz, BN-N-PCz and BN-N-BN displayed turn-on voltages of 4.8, 5.0 and 4.4 V (Vturn-on at 1.0 cd m^{-2}), respectively. In addition, the EL emission peaks and FWHMs were in good consistency with their PL profiles. For emitters BN-N-TTz and BN-N-PCz, blue-green light emissions with sharp peaks at 490 nm were observed for their devices. More importantly, their EL spectra showed narrow FWHMs of only 28 nm (0.14 eV). However, the device based on BN-N-BN exhibited bright green light emission at 530 nm. Unfortunately, its EL spectrum showed a wider FWHM of 77 nm (0.33 eV), which is due to the characteristics of the co-facial dimer structure resembling an excimer-like state (S_{exc}). The devices based on these emitters achieved the best EL performance at doping concentrations of 1 wt%, exhibiting excellent efficiency performances, with maximum EQE, CE and PE of 25.2%, 48.1 cd A^{-1} and 29.1 lm W^{-1} for BN-N-TTz, 19.5%, 36.5 cd A^{-1} and 20.9 lm W^{-1} for BN-N-PCz, and 27.6%, 100.5 cd A^{-1} and 65.8 lm

Table 3 Summary of the EL data of the investigated compound-based devices

Emitter	$\lambda_{EL}{}^a$ [nm]	$V_{on}{}^b$ [V]	$L_{max}{}^c$ [cd m^{-2}]	EQE^d [%]	CE^e [cd A^{-1}]	PE^f [lm W^{-1}]	FWHM^g [nm eV^{-1}]	CIE^h (x, y)
BN-N-TTz	490	4.8	5274	25.2/19.3	48.1	29.1	28/0.14	(0.09, 0.41)
BN-N-PCz	490	5.0	5243	19.5/16.4	36.5	20.9	28/0.14	(0.09, 0.41)
BN-N-BN	530	4.4	6606	27.6/21.6	100.5	65.8	77/0.33	(0.27, 0.61)

[a] Wavelength of the electroluminescence peak. [b] Turn on voltage at 1 cd m^{-2}. [c] Maximum luminance. [d] Maximum external quantum efficiency, and values at 100 cd m^{-2}. [e] Maximum current efficiency. [f] Maximum power efficiency. [g] Full-width at half-maximum. [h] Commission Internationale de l'Eclairage coordinates.

W^{-1} for BN-N-BN. These devices exhibit considerable efficiency performances, which can be attributed to their corresponding doped films simultaneously having high PLQYs (91%, 87% and 93% for BN-N-TTz, BN-N-PCz and BN-N-BN, respectively). Furthermore, since the morphology of the emissive layer is also important for OLED device performance, we investigated this property of CBP films doped with BN-N-TTz, BN-N-PCz and BN-N-BN at concentrations of 1.0 wt% using an atomic force microscope (AFM). As shown in Fig. S12, the BN-N-TTz and BN-N-BN doped films exhibited much smaller root-mean-square (RMS) roughness than the BN-N-PCz doped film. In particular, the results showcase the exceptional morphological stability of BN-N-TTz, as evidenced by its smaller RMS value of 0.42 nm, indicating excellent film-forming quality and superior solution processing properties. Compared to BN-N-TTz and BN-N-BN, the device based on BN-N-PCz exhibits inferior performance, which is primarily attributed to its low PLQY and poor film morphology. In addition, at a practical brightness of 100 cd m−2, the devices retain 19.3%, 16.4% and 21.6% EQE for BN-N-TTz, BN-N-PCz and BN-N-BN, respectively, corresponding to roll-offs of 23%, 16% and 22% relative to their peak values. These moderate efficiency losses, which fall below the 30–50% decay typically observed in solution-processed MR-TADF OLEDs, arise from the high RISC rates in the doped films,[26,36–38] indicating that exciton-induced degradation has been partially suppressed. As summarized in Fig. 7f and Table S2, to our delight, among the EQEs of reported solution-processed OLEDs based on MR-TADF molecules with EL peaks in the range of 400–650 nm, we note that the EQEmax efficiency of the devices based on BN-N-TTz, BN-N-PCz and BN-N-BN is outstanding, which demonstrates the success of our strategy to develop highly efficient solution-processible small-molecule MR-TADF emitters.

Conclusions

In summary, we propose a simple and feasible approach to develop high-performance solution-processible MR-TADF emitters with a U-shaped molecular structure. By reasonably designing the U-shaped molecular structure to enhance the solubility and RISC rate of emitters, BN-N-BN could reach a k_{RISC} of 3.17 × 105 s^{-1}. The solution-processed devices based on BN-N-TTz and BN-N-PCz emitters achieved excellent EL performance with EQEs reaching 25.2% and 19.5%, respectively. More encouragingly, the solution-processed device based on the BN-N-BN emitter achieved a maximum EQE of 27.6%, setting a record for solution-processed BN-resonant molecule OLEDs. This work provides important insights for the development of high-performance solution-processible MR-TADF emitters.

Author contributions

Conceptualization: X. Yang and Y. Sun; methodology: G. Zhou, X. Yang, Y. Sun and Z. Chen; validation: S. Xu, W. Liu, A. Yan and X. Du; formal analysis: S. Xu, A. Yan, X. Du, W. Liu, and J. Tao; investigation: S. Xu, A. Yan, X. Du, W. Liu, and J. Tao; resources: X. Yang, Y. Sun and Z. Chen; data curation: S. Xu, A. Yan, X. Du and W. Liu; writing – original draft preparation: S. Xu, W. Liu, X. Yang and Y. Sun; writing – review & editing: S. Xu, W. Liu, X. Yang and Y. Sun; visualization: S. Xu, A. Yan, X. Du and W. Liu; supervision: X. Yang, Y. Sun and Z. Chen; project administration: X. Yang and Y. Sun; funding acquisition: G. Zhou, X. Yang and Y. Sun.

Conflicts of interest

The authors declare no conflict of interest.

Data availability

CCDC 2485143 and 2485149 contain the supplementary crystallographic data for this paper.[39a,b]

The data supporting the findings of this study are available within the paper and the SI. Supplementary information is available. See DOI: **https://doi.org/10.1039/d5sc04507j**.

Acknowledgements

This work was supported by the National Natural Science Foundation of China (22375158 and 22175137), the Key Research and Development Program of Shaanxi (2025CY-YBXM-148), the Natural Science Foundation of Shaanxi Province (2023-JC-QN-0144), and the Fundamental Research Funds for the Central Universities (xzy012023039). The characterization assistance from the Instrument Analysis Center of Xi'an Jiaotong University is also acknowledged.

Notes and references

1 X. Zhang and H. Xu, *Angew. Chem., Int. Ed.*, 2024, **63**, e202317597.

2 S. W. Lee, S. H. Cho, H. S. Kang, G. Kim, J. S. Kim, B. Jeong, E. H. Kim, S. Yu, I. Hwang, H. Han, T. H. Park, S.-H. Jung, J. K. Lee, W. Shim and C. Park, *ACS Appl. Mater. Interfaces*, 2018, **10**, 13757–13766.

3 X. Xue, B. Zhu, Z. Kang, X. Chi, H. Zhang, A. Tang and W. Ji, *Laser Photonics Rev.*, 2025, **19**, 2401166.

4 S. Banerjee, P. Singh, P. Purkayastha and S. Kumar Ghosh, *Chem. Asian J.*, 2025, **20**, e202401291.

5 Y. Huang, E.-L. Hsiang, M.-Y. Deng and S.-T. Wu, *Light Sci. Appl.*, 2020, **9**, 105.

6 Q. Wei, Z. Ge and B. Voit, *Macromol. Rapid Commun.*, 2019, **40**, 1800570.

7 T. Huang, W. Jiang and L. Duan, *J. Mater. Chem. C*, 2018, **6**, 5577–5596.

8 H. Lee, D. Karthik, R. Lampande, J. H. Ryu and J. H. Kwon, *Front. Chem.*, 2020, **8**, 373.

9 Y. Xu, Q. Wang, X. Cai, C. Li, S. Jiang and Y. Wang, *Angew. Chem., Int. Ed.*, 2023, **62**, e202312451.

10 J.-M. Teng, Y.-F. Wang and C.-F. Chen, *J. Mater. Chem. C*, 2020, **8**, 11340–11353.

11 Y. Kondo, K. Yoshiura, S. Kitera, H. Nishi, S. Oda, H. Gotoh, Y. Sasada, M. Yanai and T. Hatakeyama, *Nat. Photonics*, 2019, **13**, 678–682.

12 R. K. Konidena and K. R. Naveen, *Adv. Photonics Res.*, 2022, **3**, 2200201.

13 S. Madayanad Suresh, D. Hall, D. Beljonne, Y. Olivier and E. Zysman-Colman, *Adv. Funct. Mater.*, 2020, **30**, 1908677.

14 P. Li, W. Li, Y. Zhang, P. Zhang, X. Wang, C. Yin and R. Chen, *ACS Mater. Lett. Letters*, 2024, **6**, 1746–1768.

15 M. Mamada, M. Hayakawa, J. Ochi and T. Hatakeyama, *Chem. Soc. Rev.*, 2024, **53**, 1624–1692.

16 Y. Feng, Y. Xu, C. Qu, Q. Wang, K. Ye, Y. Liu and Y. Wang, *Adv. Mater.*, 2024, **36**, 2403061.

17 E. Ravindran, H. E. Baek, H. W. Son, J. H. Park, Y.-H. Kim and M. C. Suh, *Adv. Funct. Mater.*, 2023, **33**, 2213461.

18 Y. Qi, W. Ning, Y. Zou, X. Cao, S. Gong and C. Yang, *Adv. Funct. Mater.*, 2021, **31**, 2102017.

19 Z. Yang, S. Li, L. Hua, S. Ying, Y. Liu, Z. Ren and S. Yan, *Chem. Sci.*, 2025, **16**, 3904–3915.

20 X. Wang, T. Hua, N. Li, G. Chen, Z. Chen, J. Miao, X. Cao and C. Yang, *Chem. Sci.*, 2025, **16**, 7495–7502.

21 X. Cai, J. Wei, Z. Li, Y. Pu, Y. Wu and Y. Wang, *Chem. Sci.*, 2025, **16**, 11539–11547.

22 R. W. Weerasinghe, S. Madayanad Suresh, D. Hall, T. Matulaitis, A. M. Z. Slawin, S. Warriner, Y.-T. Lee, C.-Y. Chan, Y. Tsuchiya, E. Zysman-Colman and C. Adachi, *Adv. Mater.*, 2024, **36**, 2402289.

23 X. Cai, Y. Pan, C. Li, L. Li, Y. Pu, Y. Wu and Y. Wang, *Angew. Chem., Int. Ed.*, 2024, **63**, e202408522.

24 G. Meng, H. Dai, T. Huang, J. Wei, J. Zhou, X. Li, X. Wang, X. Hong, C. Yin, X. Zeng, Y. Zhang, D. Yang, D. Ma, G. Li, D. Zhang and L. Duan, *Angew. Chem., Int. Ed.*, 2022, **61**, e202207293.

25 N. Ikeda, S. Oda, R. Matsumoto, M. Yoshioka, D. Fukushima, K. Yoshiura, N. Yasuda and T. Hatakeyama, *Adv. Mater.*, 2020, **32**, 2004072.

26 X. Cai, Y. Xu, Y. Pan, L. Li, Y. Pu, X. Zhuang, C. Li and Y. Wang, *Angew. Chem., Int. Ed.*, 2023, **62**, e202216473.

27 T. Wang, X. Yin, X. Cao and C. Yang, *Angew. Chem., Int. Ed.*, 2023, **62**, e202301988.

28 X.-F. Luo, X. Xiao and Y.-X. Zheng, *Chem. Commun.*, 2024, **60**, 1089–1099.

29 X. Xiong, J.-Q. Li, T.-F. Chen, X.-C. Fan, Y.-C. Cheng, H. Wang, F. Huang, H. Wu, J. Yu, X.-K. Chen, K. Wang and X.-H. Zhang, *Adv. Funct. Mater.*, 2024, **34**, 2313726.

30 Z. Chen, D. Liu, M. Li, Y. Jiao, Z. Yang, K. Liu and S.-J. Su, *Adv. Funct. Mater.*, 2024, **34**, 2404278.

31 Y. Gao, Y. Sun, Z. Guo, G. Yu, Y. Wang, Y. Wan, Y. Han, W. Yang, D. Zhao and X. Ma, *Chem. Sci.*, 2024, **15**, 18431–18442.

32 Y. Xu, C. Li, Z. Li, Q. Wang, X. Cai, J. Wei and Y. Wang, *Angew. Chem., Int. Ed.*, 2020, **59**, 17442–17446.

33 Z. Huang, H. Xie, J. Miao, Y. Wei, Y. Zou, T. Hua, X. Cao and C. Yang, *J. Am. Chem. Soc.*, 2023, **145**, 12550–12560.

34 P. Roy, G. Bressan, J. Gretton, A. N. Cammidge and S. R. Meech, *Angew. Chem., Int. Ed.*, 2021, **60**, 10568–10572.

35 C.-W. Ju, B. Li, L. Li, W. Yan, C. Cui, X. Ma and D. Zhao, *J. Am. Chem. Soc.*, 2021, **143**, 5903–5916.

36 W. Luo, T. Wang, Z. Huang, H. Huang, N. Li and C. Yang, *Adv. Funct. Mater.*, 2024, **34**, 2310042.

37 Y. Chang, K. Zhang, L. Zhao, X. Wang, S. Wang, S. Shao and L. Wang, *Angew. Chem., Int. Ed.*, 2025, **64**, e202415607.

38 S. H. Park, N. Y. Kwon, C. W. Koh, J. Y. Park, M. J. Kang, H. Kwak, C. Y. Park, S. Park, M. J. Cho and D. H. Choi, *Chem. Eng. J.*, 2024, **481**, 148484.

39 (*a*) S. Xu, W. Liu, A. Yan, X. Du, Y. Sun, J. Tao, G. Zhou, Z. Chen, X. Yang, CCDC 2485143: Experimental Crystal Structure Determination, 2025, DOI: 10.5517/ccdc.csd.cc2pdzx0; (*b*) S. Xu, W. Liu, A. Yan, X. Du, Y. Sun, J. Tao, G. Zhou, Z. Chen, X. Yang, CCDC 2485149: Experimental Crystal Structure Determination, 2025, DOI: 10.5517/ccdc.csd.cc2pf038.